

Anisotropic magneto-thermal transport in Co_2MnGa thin films

Philipp Ritzinger,¹ Helena Reichlova,¹ Dominik Kriegner,^{2,3} Anastasios Markou,³
 Richard Schlitz,^{4,1} Michaela Lammel,⁴ Gyu Hyeon Park,⁴ Andy Thomas,⁴
 Pavel Středa,² Claudia Felser,³ Sebastian T. B. Goennenwein,^{1,5} and Karel Výborný²

¹*Institut für Festkörper- und Materialphysik and
 Würzburg-Dresden Cluster of Excellence ct.qmat,
 Technische Universität Dresden, 01062 Dresden, Germany**

²*Institute of Physics ASCR, v.v.i., Cukrovarnická 10, 162 53, Praha 6, Czech Republic*

³*Max Planck Institute for Chemical Physics of Solids,
 Nöthnitzer Straße 40, 01187 Dresden, Germany*

⁴*Leibniz Institute for Solid State and Materials Research Dresden (IFW Dresden),
 Institute for Metallic Materials, 01069 Dresden, Germany*

⁵*Department of Physics, University of Konstanz,
 Universitätsstrasse 10, 78457 Konstanz, Germany*

(Dated: Dec22, 2020)

Abstract

Ferromagnetic Co_2MnGa has recently attracted significant attention due to effects related to non-trivial topology of its band structure, however a systematic study of canonical magneto-galvanic transport effects is missing. Focusing on high quality thin films, here we systematically measure anisotropic magnetoresistance (AMR) and its thermoelectric counterpart (AMTP). We model the AMR data by free energy minimisation within the Stoner–Wohlfarth formalism and conclude that both crystalline and non-crystalline components of this magneto-transport phenomenon are present in Co_2MnGa . Unlike the AMR which is small in relative terms ($\sim 0.1\%$), the AMTP is large due to a change of sign of the Seebeck coefficient as a function of temperature. This fact is discussed in the context of the Mott rule and further analysis of AMTP components is presented.

* Corresponding author: philipp.ritzinger@web.de

Electron transport phenomena in magnetically ordered materials span a vast range both historically and from the point of view of complexity. While some of them which have been known for a long time, such as the anisotropic magnetoresistance (AMR) [1], remain a subject of roughly constant interest until today [2–4] others rose to prominence only recently. Such is the case of the anomalous Nernst effect [5] (ANE) for example, an outstanding member of the field of spin caloritronics [6]. In a typical thin film geometry with magnetic field applied in the direction normal to the film plane and a thermal gradient in the sample plane, the ANE signal is detected in the other (perpendicular) in-plane direction. This effect is particularly strong in ferromagnetic Co_2MnGa [7] (identified as a Weyl semimetal [8]) and having thus drawn considerable interest it has been investigated in sufficient detail already [9–11].

In this work, we extend the discussion also to effects which occur when magnetic field is applied in the sample plane. The studied thin film of Heusler alloy Co_2MnGa represents an ideal model system because of its high crystalline quality, relatively strong magneto-thermal response, its high Curie temperature ($T_C = 694$ K) and high spin polarisation [12]. We study systematically the magneto-thermal transport response when the magnetic field is rotated in three perpendicular rotation planes. Along with AMR, the anisotropic magneto-thermopower (AMTP) is reported and compared qualitatively. We discuss the applicability of a simple Stoner–Wohlfarth-based model (as used recently in a different context, for example in Ref. [3]) to the AMTP data and compare the ratio of amplitudes of AMTP and AMR in various samples and at different temperatures. We report crystalline contributions to both AMR and AMTP and interestingly, some of these seem missing (or at least they are significantly weaker) in the latter effect. Inconsistencies related to the straightforward application of the Mott rule to our measurements suggest a sizable phonon [13] or magnon [14] drag contribution to the thermopower.

This paper is structured as follows: in Sec I we are motivating the comparison of anisotropic magnetoresistance (AMR) and anisotropic magnetothermopower (AMTP) and provide some background on these two effects. In Sec II, the formalism used for the data analysis is introduced and sample fabrication and characterisation is described in Sec. III. Finally, experimental results are shown and discussed in Sec. IV; an outlook and and summary is provided in Sec. V.

I. INTRODUCTION

Both AMR and AMTP refer to voltage variation as a function of the angle between magnetization and the driving force (electrical current \mathbf{j} in case of AMR and temperature gradient ∇T in case of AMTP) or the angle between magnetization and the crystal axes in the respective setting. Although they could probe similar physical properties, there are many more reports about AMR than about AMTP, mostly due to experimental challenges in measuring AMTP. In the following, we give a brief introduction of both.

Since the original observation of AMR by William Thomson [1] the AMR is typically understood as a variation of resistance as a function of magnetisation \mathbf{M} direction [15] $\Delta\rho_{yy}(\varphi) = C_I \cos 2\varphi$, with φ denoting the angle between current and magnetisation. However, there is another level of complexity in AMR. In 1938, the discussion of this effect was extended to the influence of crystalline symmetry. W. Doering [16] carried out symmetry-based AMR analysis [17] of resistivity tensor using a series expansion up to fourth order in powers of the direction cosines of the magnetization. These expansions contain AMR terms different from the "non-crystalline" $\cos 2\varphi$ ones and such additional terms are sometimes called "crystalline" AMR since they reflect the crystal symmetry and not the symmetry breaking induced by the electrical current direction. Consequently, unlike the non-crystalline AMR, the crystalline AMR contributions can be non-zero even if $\varphi = \pi/2$ remains constant (for example, during the magnetic field rotation in the plane perpendicular to \mathbf{j}). Such a situation will be discussed in the experimental setup sketched in Fig. 2(e) below.

AMTP is the thermoelectrical counterpart of AMR. The basic phenomenon (voltage drop induced by a temperature gradient) was discovered by T.J. Seebeck already in 1821, thus establishing the field of thermoelectrics. Hints at its anisotropy came much later [18] however and since then, AMTP has attracted relatively small attention compared to the AMR. Nevertheless, increasing global demand for energetically sustainable solutions [19] and the need of advanced microscopy techniques [20] sparked new interest in this effect.

Recent thermoelectric studies in solid state magnetism focus mostly on the evaluation of Σ (the Seebeck coefficient [21]) or the anomalous Nernst effect (ANE) [6]. The Seebeck coefficient provides information about the charge carriers, such as concentration, effective mass or dominant type (electrons or holes) and ANE stirs interest due to the connection to band structure topology [22] and better technological prospects in thermoelectric energy

harvesting [23]. In addition to the ANE, the Seebeck coefficient anisotropy comes with the possibility for its tensor components Σ_{xy} and Σ_{yy} to depend on the magnetic field direction: the anisotropic magneto-thermopower (AMTP) which is a direct analog to the non-crystalline AMR, can be expressed as

$$\begin{aligned}\Sigma_{xy} &= S_I \sin 2\varphi && \text{accompanied by} \\ \Delta\Sigma_{yy} &= S_I \cos 2\varphi, && (1)\end{aligned}$$

where $\Delta\Sigma_{yy}$ is the difference between Σ_{yy} and its average. These relations pertinent to polycrystalline materials can be straightforwardly derived by angular averaging the Seebeck tensor as given by Eq. 3.31 in Ref. [24] and we also discuss this relationship in Sec. III.

In contrast to ANE, the AMTP is rarely a topic of systematic studies; with few exceptions [25, 26] reports are usually limited to assume its existence (in longitudinal [27, 28] or transversal [18, 29] geometry also known as the planar Nernst effect) and the AMTP often assumes the role of an unwanted artefact. The main reasons are the notorious difficulty to precisely quantify direction and amplitude of a thermal gradient and small magnitude of the measured thermo-voltages, typically on resolution limit of a common laboratory equipment. This makes the AMTP experiment significantly more challenging than a simple resistivity measurement with a well-defined current direction. The thermal gradient quantification is even more complex in thin film samples where the substrate acts as a heat sink. The lack of detailed understanding of AMTP becomes obvious when considering systems with various contributions to AMR. In particular, very few reports show more complex symmetry of AMTP [25], the existence of a crystalline component in the AMTP is not yet established and a comparison between the crystalline contributions to AMR and AMTP is entirely missing. The understanding of AMTP is not only a fundamental scientific question, but it is equally important in order to exclude various artefacts in experiments during which thermal gradient is unintentionally generated.

II. SAMPLE FABRICATION AND CHARACTERIZATION

The Co_2MnGa thin-film samples are fabricated by magnetron sputtering on $\text{MgO}(001)$ substrates using a multisource Bestec UHV deposition system from Co, Mn and MnGa sputter targets. Growth and post-growth annealing was performed at 500°C . After the

Co₂MnGa thin-film growth, 3 nm of Al were deposited at room temperature to prevent oxidation. Further details of the growth procedure can be found elsewhere [30]. Here, two samples showing highest crystal quality with Co₂MnGa thickness of 40 nm and 50 nm are studied. The chemical composition and structural investigation conducted by X-ray diffraction techniques showed Bragg peaks corresponding to the material composition revealing a high degree of atomic order similar to Refs. [9, 30]. Figure 1(c) shows the symmetric radial X-ray diffraction scans, which includes diffraction from lattice planes parallel to the substrate surface. Given the epitaxial alignment of Co₂MnGa(001)[110] || MgO(001)[100], i.e. an in-plane 45° degree rotation, only the 00*L* Bragg peaks are visible in Fig. 1(c). Well defined, narrow Bragg peaks evidence the good chemical homogeneity and crystal quality. While bulk Co₂MnGa has a cubic L2₁ crystal structure the thin-films exhibit an epitaxial strain-induced tetragonal distortion with slight contraction along the out of plane [001] direction. Resulting *c/a* ratio is around 0.99 [30]. Figure 1(d) shows X-ray reflectivity data of the 40 nm and 50 nm thick Co₂MnGa epilayer displaying Kiessig fringes that extend beyond the measurement range. This bears witness to a low surface and interface roughness which were determined to be below 7 Å by modelling using an extended Parratt formalism [31].

Magnetization of these epilayers was measured in a SQUID magnetometer, which is shown in Fig. 1(b). The saturation magnetic moment of about 4 μ_B / f.u. is consistent with literature (saturation magnetisation M_{sat} 720 kA/m) [9, 11]. The films were patterned into 40 μm wide Hall bars by optical lithography and by a combination of HCl and Ar/O₂ plasma etching. A schematic image of the sample is shown in Fig. 1(a). After the etching, the heater and thermometers were fabricated in a lift-off process with 30 nm of sputtered Pt. Platinum wires, highlighted as pink areas in Fig. 1(a), at the top of the Hall bar serve as on-chip heater, while platinum wires at the side work as an on-chip thermometer (green areas).

Experimental Setup

In the AMR experiments, a sufficiently strong magnetic field ($\mu_0 H = 1.5$ T stronger than $M_{\text{sat}} \approx 0.9$ T and the anisotropy field ≈ 0.6 T corresponding to k_u) is rotated in three rotation planes called XY, ZY and ZX plane as shown in Fig. 2 (a), (c) and (e). Current $I = 0.2$ mA (corresponding to current density 1.2×10^6 A/cm²) is applied along the y-axis. At each step of the magnetic field rotation, data is collected for $I = +0.2$ mA and for

$I = -0.2$ mA and averaged, in order to cancel out the thermoelectric contributions, which occur in form of voltage offsets. The experiments are conducted at different temperatures between 10 K and 300 K. The data are shown as symbols in Fig. 2.

In the AMTP experiments, magnetic field is rotated in the same rotation planes XY, ZY and ZX. The experiments are conducted at several temperatures between 100 and 300 K; at lower temperatures the AMTP signal decreases below the resolution owing to the decrease of entropy.

The thermometers are first calibrated by sweeping the temperature of the cryostat from low temperature to room temperature and using a Cernox thermometer in the cryostat as a reference. At each studied temperature, a constant current of $I_{\text{thermom}} = 0.1$ mA is applied on the on-chip thermometers (platinum wires, green areas in Fig 1), while the measured voltage serves as measure of the temperature. Thermal gradient is generated by Joule heating of the heater, typically we apply a current of $I_{\text{heater}} = 17.5$ mA. The on-chip thermometry allowed us to determine the thermal gradient ∇T , which is 0.4 K/mm at $T = 100$ K and 0.5 K/mm at 200 K - 300 K [9]. In order to reduce noise, the magnetic field was rotated several times and at each rotation step, several voltage measurements are taken. In addition, the presented data are averaged over several magnetic field rotations. Since the thermal gradient takes long time to stabilise, it was not reversed at each step of the rotation as in the case of the AMR.

III. PHENOMENOLOGICAL MODEL

The phenomenological model used in this work was previously employed by Limmer et al. [24, 32] for AMR in (Ga, Mn)As and extended to AMTP in the same material system by Althammer [25] and we present a brief summary here. Similar schemes are used also in the context of AMR in antiferromagnets. [3]

Coordinate system is chosen as follows: \mathbf{z} is the surface normal vector, which is in the $[0\ 0\ 1]$ direction, electric field and thermal gradient are applied along $[1\ 1\ 0]$ denoted by \mathbf{y} and $\mathbf{x} = \mathbf{y} \times \mathbf{z}$. A sketch of the Hall bar with the coordinate system is shown in Fig 1(a).

The basic simplifying assumption is that magnetisation \mathbf{M} is saturated (which is plausible given the very narrow hysteresis loop shown in Fig. 1(b) and that we are in a single-domain state. Stoner-Wohlfarth (SW) model [33] can then be used to infer the magnetisation di-

rection $\mathbf{m} = \mathbf{M}/M_{\text{sat}}$ (here, M_{sat} is the saturation magnetisation) for any given applied magnetic field \mathbf{H} by minimizing the free energy density F . We note that this approach is capable of reproducing hysteresis effects but these never occur in the parameter range of interest here. Both the Zeeman energy and magnetic anisotropies contribute to F and the latter in Co_2MnGa shows a cubic anisotropy k_c and an uniaxial anisotropy k_u which is expected due to demagnetization energy and substrate-induced strain. With μ_0 being the vacuum permeability, we use $F = -\mu_0\mathbf{H} \cdot \mathbf{M} + k_u m_z^2$ because the cubic anisotropy can be neglected (FMR measurements [34] show that it is two orders of magnitude smaller than the applied magnetic field).

The resistivity tensor is obtained by making a series expansion in powers of cartesian components of \mathbf{m} up to the fourth order. This ansatz was first developed by Birss and Muduli et al. and applied for example [32] to $(\text{Ga}, \text{Mn})\text{As}$. The tensor writes as:

$$\rho_{ij}(\mathbf{m}) = \rho_{ij}^{(0)} + \rho_{ijk}^{(1)} m_k + \rho_{ijkl}^{(2)} m_k m_l + \rho_{ijklm}^{(3)} m_k m_l m_m + \rho_{ijklmn}^{(4)} m_k m_l m_m m_n + \dots \quad (2)$$

where $\rho_{ij}^{(0)}$, $\rho_{ijk}^{(1)}$, $\rho_{ijkl}^{(2)}$, $\rho_{ijklm}^{(3)}$ and $\rho_{ijklmn}^{(4)}$ are the expansion coefficients and magnetisation direction components $m_n \in \{m_{[100]}, m_{[010]}, m_{[001]}\}$.

The number of independent parameters is reduced owing to $m_k m_l = m_l m_k$, the Onsager relation $\rho_{ij}(\mathbf{m}) = \rho_{ji}(-\mathbf{m})$ and Neumann's principle [35] pertaining to the crystal symmetry. The last mentioned is tetragonal in our case, whereas the tetragonal axis is in z -direction, since the thin-film samples are strained by the MgO substrate (see Sec. II). The complete form of the resistivity tensor is not needed for the further process and can be found in the Appendix. The longitudinal resistivity ρ_{long} is obtained by projecting the resistivity tensor ρ along the current direction by making use of Ohm's law $\mathbf{E} = \rho \cdot \mathbf{J}$ and $E_{\text{long}} = \mathbf{j} \cdot \mathbf{E}$, where \mathbf{J} is the current density vector and $\mathbf{j} = \mathbf{J}/J$ is the corresponding unit vector, in our case $\mathbf{j} = \frac{1}{\sqrt{2}}(1, 1, 0) = \mathbf{y}$. The projection writes as:

$$\rho_{\text{long}} = \rho_{yy} = \mathbf{j} \cdot \rho \cdot \mathbf{j} \quad (3)$$

The longitudinal resistivity ρ_{yy} in our configuration is therefore given by:

$$\rho_{yy} = \rho_0 + a_{y2} \cdot m_y^2 + a_{z2} \cdot m_z^2 + a_{y4} \cdot m_y^4 + a_{z4} \cdot m_z^4 + a_{zy2} \cdot m_z^2 \cdot m_y^2 \quad (4)$$

where ρ_0 is the offset resistivity, a_{y2} and a_{z2} are the coefficients of the lowest-order AMR terms, a_{y4} , a_{zy2} and a_{z4} are the coefficients of the higher-order AMR terms and m_y and m_z are the y - and z -component of \mathbf{m} in the coordinate system $\{x, y, z\}$ as introduced above.

The derivation of the longitudinal Seebeck coefficient Σ_{yy} is analogous to the resistivity. The only difference is here that the Onsager relation connects the Seebeck tensor with the Peltier tensor and thus cannot be used to reduce the number of independent parameters. Hence, Σ_{yy} contains an additional term:

$$\Sigma_{yy} = \Sigma_0 + s_{y2} \cdot m_y^2 + s_{z2} \cdot m_z^2 + s_{zyx} \cdot m_z \cdot m_y \cdot m_x + s_{zy2} \cdot m_z^2 \cdot m_y^2 + s_{y4} \cdot m_y^4 + s_{z4} \cdot m_z^4 \quad (5)$$

where analogously Σ_0 is the thermoelectric offset, s_{y2} and s_{z2} are the coefficients of the lowest-order AMTP terms and s_{y4} , s_{z4} , s_{zy2} and s_{zyx} are the coefficients of the higher-order AMTP terms. Since the magnetic field is going to be rotated in either the XY-, the ZY- or the ZX-plane and amongst the anisotropies only the out-of-plane uniaxial term is significant, one of the m_i is in every plane expected to be zero (e.g. m_x in the ZY-plane), the term $m_z \cdot m_y \cdot m_x$ is expected to be zero in every of our rotation planes and is thus ignored. Hence, the AMR and AMTP formulae contain the same terms *in our measurement setup*. We note that for polycrystals, only the first two terms in Eq. (5) remain and moreover, $\frac{1}{2}s_{y2} = S_I$ Eq. (1). In other words, all other terms in Eq. (5) can be classified as crystalline AMTP.

In the following, we will analyse experimental AMR and AMTP data using Eqs. (4) and (5) combined with the SW model which provides a link between external magnetic field and magnetisation $\mathbf{m} = (m_x, m_y, m_z)$ that enters those equations. The final results of the fitting procedure are depicted in Fig. 2. It will be shown in Fig. 3 that for AMR, all terms in Eq. (4) need to be retained lest the quality of fits deteriorate significantly in some measurement configurations. On the other hand, the last three terms of Eq. (5) are not needed for a good fit of AMTP; s_{zyx} cannot be inferred from our data as already mentioned.

IV. RESULTS

Experimental data (symbols) and fits using the phenomenological model (lines) for both AMR and AMTP in the 50 nm sample are shown in panels (b), (d) and (f) of Fig. 2. While the AMR and AMTP data, with suitable scaling, seem alike in panels (b) and (d), the rotation of \mathbf{M} in the plane perpendicular to \mathbf{j} (see Fig. 2f) gives a different picture. We elaborate on this finding below and only note here, that in the latter configuration, non-crystalline terms [15] do not contribute to the measured AMR and AMTP which will now be discussed separately.

AMR Quantity	40 nm	50 nm	40 nm	50 nm	AMTP Quantity
ρ_0 [$\mu\Omega$ cm]	185.2	186.0	-15.57	-6.61	Σ_0 [$\mu\text{V}/\text{K}$]
a_{y2} [$\mu\Omega$ cm]	-0.730	-0.267	-0.216	-0.248	s_{y2} [$\mu\text{V}/\text{K}$]
a_{z2} [$\mu\Omega$ cm]	-0.229	0.046	0.270	0.283	s_{z2} [$\mu\text{V}/\text{K}$]
a_{y4} [$\mu\Omega$ cm]	0.155	0.064	-	-	s_{y4} [$\mu\text{V}/\text{K}$]
a_{z4} [$\mu\Omega$ cm]	-0.242	-0.106	-	-	s_{z4} [$\mu\text{V}/\text{K}$]
a_{zy2} [$\mu\Omega$ cm]	0.008	0.008	-	-	s_{zy2} [$\mu\text{V}/\text{K}$]

TABLE I. Fitted AMR and AMTP parameters at room temperature.

AMR

The phenomenological fit to AMR data (blue crosses in Fig. 2) takes into account the uniaxial magnetic anisotropy k_u , lowest-order terms a_{y2} and a_{z2} and also higher-order AMR terms a_{y4} , a_{z4} and a_{zy2} . Eq. (4) combined with k_u of the SW model resulted in a very good agreement between the data and model. On the other hand, fits omitting the higher-order crystalline terms (specifically, a_{y4} , a_{z4} and a_{zy2}) shown on the left of Fig. 3 lead to a clear trace of the omitted terms in the residuals. Such a reduced form of Eq. (4) does not allow to reproduce the data well, even when a cubic magnetization anisotropy is included in the SW model (not shown in Fig. 3). The obtained AMR parameters corresponding to $T = 300$ K (RT) are shown in Tab. I.

Inferred RT values of k_u (438 and 416 kJ/m³ for the 40 and 50 nm sample, respectively) are in a good agreement with ferromagnetic resonance measurements carried out independently [34] and the temperature dependence of such magnetic anisotropy, see Fig. 4(a), is consistent [36] with that of the magnetisation (see Fig. 1b). Turning our attention to the transport coefficients, the largest of the AMR parameters is the in-plane lowest-order one: a_{y2} . It is negative, which reflects that the resistivity is smaller for $\mathbf{m} \parallel \mathbf{j}$ than for $\mathbf{m} \perp \mathbf{j}$, a situation commonly referred to as *negative AMR* [37]. This is opposite to what is found in more common ferromagnets such as iron, nickel, cobalt and their alloys [38] and more importantly, it is also consistent with the finding of Sato et al. [39] who found a negative AMR ratio $(\rho_{\parallel} - \rho_{\perp})/\rho_{\perp}$ in Co₂MnGa for current along [1 1 0]. Some other ferromagnetic systems, (Ga,Mn)As for instance [15], carry negative AMR too.

Temperature dependences of the AMR parameters are shown in Fig. 4. Their trends

for the 50 nm sample are similar to those of the 40 nm sample except for the out-of-plane lowest-order a_{z2} parameter; even so, the both data sets in Fig. 4(e) seem to have a minimum slightly below RT. According to the absolute value, the magnitude of the parameters in descending order are as follows: $|a_{y2}| > |a_{z4}| > |a_{z2}| > |a_{y4}| > |a_{zy2}|$.

Such observations, however, lack any universal validity. Trends regarding the order of magnitude or the sign of the coefficients can be observed, yet they cannot be generalized. This is also confirmed by results of similar studies in Co_2FeAl [25] and in $(\text{Ga}, \text{Mn})\text{As}$ [24, 25, 32]. Hence, there are always exceptions to a rule: $|a_{y2}|$ is usually the largest of the AMR coefficients (but not for very thin samples [40]) and a_{y4} is in most cases positive (but not at very low temperatures in the 50 nm sample) to give two examples. Since our model is phenomenological and the microscopic origins of the AMR mechanisms are not fully understood for Co_2MnGa , an explanation of the observed behaviour remains an open question.

Attempts to identify the underlying mechanisms of AMR in related materials have been undertaken by Kokado and Tsunoda [41] whereas the focus was on electron scattering. They used a two-current model, taking into account s -to- s and s -to- d scattering. The Hamiltonian of the localized d -states includes spin-orbit interaction, an exchange field and a crystal field of cubic or tetragonal symmetry, where the tetragonal distortion is in $[001]$ direction. They found that the a_{y4} contribution (C_4 in their notation) appears under a tetragonal symmetric crystal field, but almost vanishes under cubic symmetry. This is consistent to other studies that reported that a four-fold-contribution (a_{y4} in our notation) is not needed to describe the in-plane AMR. However, thin-films are expected to be strained by the substrate and thus to show some tetragonality, which leads to a non-zero a_{y4} contribution. On the other hand, the strain is different in each sample. Thus, studies that reported a two-fold in-plane AMR (i.e. $a_{y4} = 0$) might have samples with relatively low strain, which are almost cubic.

AMTP

To fit the AMTP data, we used a procedure analogous to fitting AMR except for the anisotropy constant k_u : this parameter has already been determined before and we now kept it fixed. Note, that due to the on-chip heating the actual temperature might be slightly different than indicated. However since the change of k_u with temperature is small, it does

not change the accuracy of our approach. Given our measurement geometry, $m_x m_y m_z = 0$ at all times, hence Eq. (5) contains the same terms as Eq. (4) and in particular, we started with the lowest-order terms s_{y2} and s_{z2} . Only these lowest-order parameters and the magnetic anisotropy were needed to obtain good fits to the AMTP data, which is a pronounced difference to the AMR. A reason for this difference could be the noise which is stronger in the AMTP data as compared to the AMR. We have not been able to achieve as good resolution as in the case of the AMR. However, the noise allows us to determine a maximum value of possible higher-order terms, which need to be smaller than the noise. In absolute terms, the noise is of the order of magnitude $0.10 \mu\text{V}/\text{K}$ and below, which implies that the higher-order symmetries are smaller than about one fifth of the lowest-order symmetries (see Tab. I). This is not only a striking difference to AMR in our samples, where lower- and higher-order coefficients are in the same order of magnitude, but also to the analysis of AMTP in (Ga, Mn)As by Althammer [25], where the existence of higher-order AMTP parameter is reported. In relative terms, the noise shown in Fig. 3 (as residuals after subtracting the fits from experimental data) is large which is a consequence of difficulties in controlling the temperature gradient under experimental conditions. The temperature evolution of the AMTP parameters as well as a comparison to the lowest-order AMR parameters is shown in Fig. 5(b).

In Fig. 5(a), the Seebeck coefficient Σ_0 is shown as function of temperature. In literature, the Seebeck coefficient of Co_2MnGa ranges between approximately $-2\mu\text{V}/\text{K}$ and $-30\mu\text{V}/\text{K}$ at RT, whereas no clear trend is recognizable and the present measurements fall within this range: we find Σ_0 for both samples close to $-15\mu\text{V}/\text{K}$. Seebeck coefficient of the 50 nm sample is increasing in absolute value with increasing temperature, as expected from previously published experiments [42, 43].

As mentioned in Sec. I, the sign of Σ_0 is attributed to the dominant charge carrier type, which are electrons for $\Sigma_0 < 0$. A negative Seebeck coefficient is reported not only in Co_2MnGa , but in Co-based Heusler compounds in general [7]. The sign change of Σ_0 would mean that the dominant charge carrier type switches from electrons to holes for decreasing temperatures. This was shown to occur in other materials depending on the doping [44]. However, other scenarios are also plausible which we discuss in the next subsection and we now turn our attention to the AMTP.

We notice that neither s_{y2} nor s_{z2} , whose temperature dependence is shown in Fig. 5(b),

can be correlated to their AMR counterparts. While a_{z2} is decreasing with increasing temperature and the dependence of a_{y2} is non-monotonic, the AMTP parameters exhibit very different dependence, although they were measured on exactly same device in the and same structure. At $T = 250$ K in both AMTP parameters, there is an outlier. This might be due to a thermal offset variation. Together with the sign change of s_{z2} the lack of correlation between the AMR and AMTP is evident. This is in striking contrast to the transversal transport measured in the same material [11]. In that study the AHE and ANE were measured simultaneously and clear correlation was observed including the presence of outliers.

From our study it appears that comparing the lowest-order parameters, no common trend can be found between the AMR parameters and their respective AMTP counterpart when looking at the temperature dependence. Moreover, in case of the ZX rotation (see Fig. 2f), even the raw angular sweep data are clearly very different: the fourth-order terms can be basically seen by naked eye in the AMR while in the AMTP, they are apparently absent and no such terms can be identified in the residuals on right panels of Fig. 3. In the systematic study of AMR and AMTP in (Ga,Mn)As by Althammer, higher-order contributions have been found for both effects, but the parameters did not appear to be correlated with each other. Since the amount of data in this and all past studies is relatively small, further studies are desirable to investigate if any correlation between AMR und AMTP coefficients exists.

The fact, that in two different systems the AMR and the AMTP follow different trends is, however, a strong indication, that there might be a more fundamental reason behind this discrepancy such as the suppressed role of anisotropic scattering in the AMTP, which calls for further investigation; below, we discuss one possible direction of such tentative research.

Mott rule and phonon drag

Electron and heat transport linear response coefficients are tensorial quantities which obey Onsager relations [45] and combine into the Seebeck coefficient Σ_0 . To see this, we rewrite the electron transport equation as

$$\mathbf{E} = \rho \mathbf{j} + \Sigma_0 \nabla T$$

and set $\mathbf{j} = 0$. Under the assumption of elastic scattering, the Mott rule holds (still in tensorial sense)

$$\Sigma_0 = -eL_0T\rho\sigma' = eL_0T\rho'\sigma \quad (6)$$

where $\rho\sigma = 1$ and the prime denotes the derivative with respect to energy E at chemical potential. For semiconductors, this derivative can be straightforwardly accessed through carrier-density-dependent conductivity [46] but no such possibility is obvious in our metallic system. However, when resistivity is broken down into a magnetisation-independent background ρ_0 and a small correction $\Delta\rho$ that effectively constitutes the AMR, the following observation is possible.

Let us first assume that ρ which depends both on E and \mathbf{M} can be written as

$$\rho(E, \mathbf{M}) = \rho_0(E) + \Delta\rho(\mathbf{M}). \quad (7)$$

Eq. (6) can then be rewritten as $\Sigma_0 = eL_0T\rho_0'\sigma$ and since ρ_0 is a scalar quantity, it essentially implies that AMTP is proportional to the AMR (tensors Σ_0 and σ are proportional through a scalar factor). In terms of data shown in Fig. 2, this could seem to imply that dominant non-crystalline contributions of AMR (XY and ZY rotations) indeed follow while the more delicate and smaller crystalline terms (ZX rotation) break the assumption (7) and give different AMR and AMTP angular dependences.

On a careful inspection however, we notice that AMR and AMTP amplitudes in the left and middle panels of Fig. 2 are not proportional the same way as the average ρ and Σ_0 (this is made explicit by scaling of the vertical axes on the left three panels in Fig. 3). While the assumption (7) may be not accurately fulfilled (specifically, the $\Delta\rho$ term is unlikely to be perfectly energy-independent), there is also another possibility to explain this discrepancy. We note that thermopower is strongly temperature-dependent (data in Fig. 5a show that it changes almost by a factor of three between 250 and 300 K) and at the same time, ρ_0 changes only at the order of per cent in the same temperature interval.

This explanation is related to the phonon drag contribution to thermopower which is not included in the Mott formula (6). In semiconductors, this contribution can easily exceed (see Fig. 12 in Protik&Broido [13]) the electronic thermopower or, in other words, it can reach the level of 100 $\mu\text{V}/\text{K}$. It is therefore plausible that the measured (relatively small) value of Σ_0 is the result of competition of two (large, relative to Σ_0) contributions: the usual electronic contribution related to the Fermi-Dirac factor $f_{FD}(E)$ depending on temperature

and the phonon drag contribution caused by electron-phonon interaction. Once the phonon drag contribution would be removed from the measured Σ_0 , the amplitude-to-average ratio of AMTP drops to the same level as for the AMR (here, we again refer to the Fig. 2(b) and (d) consistent with proportionality of AMR and AMTP implied by the Mott formula under assumption (7). This way, our measurements suggest a sizable phonon drag effect in the thermopower of Co_2MnGa . Alternatively, magnon drag could be at works [14, 47]. Regarding Fig. 2(f) we note that quite clearly, proportionality between AMR and AMTP is by no means exact and it seems (in the view of data in Fig. 5(b) that thermopower in Co_2MnGa is more sensitive to crystallographic orientation than resistivity.

V. SUMMARY

In this study, we compared the AMR and AMTP in two Co_2MnGa -thin-film samples using a simple Free Energy density and phenomenological symmetry-based models for AMR and AMTP based on a series expansion in powers of the magnetization direction vector \mathbf{m} . We showed that non-zero resistivity-contributions up to 4th order are necessary for a sensible modeling, where in the AMTP only lowest-order contributions are necessary. The AMR and AMTP are not showing any trends in common, which is consistent with previous studies in $(\text{Ga}, \text{Mn})\text{As}$. We experimentally confirm presence of a crystalline contribution to the AMTP. It appears that the universal Mott rule validity is broken due to a discrepancy of the symmetries of AMR and AMTP in one rotation plane. This discrepancy was discussed in terms of a significant phonon (magnon) drag contribution to thermopower, which might be the origin of such a discrepancy.

The results of this study call for further enquiry: First of all, we need to broaden our understanding about the origins and governing influences in AMR, but also in AMTP. Theoretical studies discussing influences in AMTP similar to whose about AMR are desirable. Experimental studies using sets of samples which are systematic with respect to strain, composition or other influences can help us also along this way.

ACKNOWLEDGEMENTS

We thank Peter Svekis for discussions and Juliane Scheiter for technical support with magnetometer. HR acknowledges support from Christiane Nüsslein-Volhard Stiftung and funding through Würzburg–Dresden Cluster of Excellence, SFB 1143 (project ID 247310070) and FET Open RIA Grant No. 766566 also deserves a grateful mention.

Appendix A: Notes on derivation of Eqs. 4,5

Comments on the full form of $\rho^{(i)}$ in Eq. (2) are given here, from which Eq. (4) can be derived. A more detailed description can be found in Appendix A.1 of thesis [40] of one of the authors. Only terms corresponding to cubic symmetry are included and summation over repeated indexes (Einstein notation) is implied. Note that the underlying coordinate system is equivalent to the one applied in Eq. 2, thus: $m_n \in \{m_{[100]}, m_{[010]}, m_{[001]}\}$. We skip $\rho_{ijk}^{(1)}$ which does not appear in ρ_{long} the in-plane geometry (it corresponds to the anomalous Hall effect). The lowest non-trivial order thus becomes

$$\rho_{ijkl}^{(2)} m_k m_l = C_1 \begin{pmatrix} m_x^2 & 0 & 0 \\ 0 & m_y^2 & 0 \\ 0 & 0 & m_z^2 \end{pmatrix} + C_2 \begin{pmatrix} 0 & m_x m_y & m_x m_z \\ m_x m_y & 0 & m_y m_z \\ m_x m_z & m_y m_z & 0 \end{pmatrix}.$$

The third-order terms, $\rho_{ijklm}^{(3)}$, again do not contribute in Eq. (3), and the fourth-order terms $\rho_{ijklmn}^{(4)} m_k m_l m_m m_n$ become

$$E_1 \begin{pmatrix} m_x^4 & 0 & 0 \\ 0 & m_y^4 & 0 \\ 0 & 0 & m_z^4 \end{pmatrix} + E_2 \begin{pmatrix} m_y^2 m_z^2 & 0 & 0 \\ 0 & m_x^2 m_z^2 & 0 \\ 0 & 0 & m_x^2 m_y^2 \end{pmatrix} + E_3 \begin{pmatrix} 0 & m_x m_y m_z^2 & m_x m_z m_y^2 \\ m_x m_y m_z^2 & 0 & m_y m_z m_x^2 \\ m_x m_z m_y^2 & m_y m_z m_x^2 & 0 \end{pmatrix}.$$

Additional terms appear when lower symmetry is assumed, which is in our case due to the tetragonal distortion along the $\hat{z} = [001]$ axis of the thin-film samples. The following zeroth-order and second-order terms add to the resistivity tensor in the case of tetragonal symmetry:

$$\begin{pmatrix} 0 & 0 & 0 \\ 0 & 0 & 0 \\ 0 & 0 & a \end{pmatrix} + \begin{pmatrix} c_3 m_z^2 & 0 & c_2 m_x m_z \\ 0 & c_3 m_z^2 & c_2 m_y m_z \\ c_2 m_x m_z & c_2 m_y m_z & c_1 m_z^2 \end{pmatrix}$$

Under tetragonal symmetry, the fourth-order terms are supplemented by:

$$\begin{pmatrix} e_2 m_y^2 m_z^2 + e_4 m_z^4 & e_3 m_x m_y m_z^2 & e_6 m_x m_y^2 m_z + e_7 m_x m_z^3 \\ e_3 m_x m_y m_z^2 & e_2 m_x^2 m_z^2 + e_4 m_z^4 & e_6 m_x^2 m_y m_z + e_7 m_y m_z^3 \\ e_6 m_x m_y^2 m_z + e_7 m_x m_z^3 & e_6 m_x^2 m_y m_z + e_7 m_y m_z^3 & e_5 m_x^2 m_y^2 + e_1 m_z^4 \end{pmatrix}$$

In a similar (yet distinct) manner, the Seebeck tensor can be expanded, see Appendix B.1 of Ref. [40]. In the case of tetragonal symmetry, to which Eq. (5) applies, several additional terms appear but they do not contribute to Σ_{yy} except for

$$D_7 m_x m_y m_z \begin{pmatrix} -1 & 0 & 0 \\ 0 & 1 & 0 \\ 0 & 0 & 0 \end{pmatrix}$$

which gives rise to the last term in Eq. (5). Therefore even in our setup, ρ_{yy} and Σ_{yy} allow in principle for a different functional form albeit not with our constraint to XY, YZ, and XZ rotations of magnetic field. Further information can be found in Ref. [25] or in the Appendix of Ref. [40].

-
- [1] W. Thomson, Proc. R. Soc. Lond. **8**, 546-550 (1856)
 - [2] M. Wang, C. Andrews, S. Reimers, O. J. Amin, P. Wadley, R. P. Campion, S. F. Poole, J. Felton, K. W. Edmonds, B. L. Gallagher, A. W. Rushforth, O. Makarovskiy, K. Gas, M. Sawicki, D. Kriegner, J. Zubáč, K. Olejník, V. Novák, T. Jungwirth, M. Shahrokhvand, U. Zeitler, S. S. Dhesi, and F. Maccherozzi, Phys. Rev. B **101**, 094429 (2020)
 - [3] J. Volný, D. Wagenknecht, J. Železný, P. Harcuba, E. Duverger–Nedellec, R. H. Colman, J. Kudrnovský, I. Turek, K. Uhlířová, and K. Výborný, Phys. Rev. Materials **4**, 064403 (2020).
 - [4] Y. Miao, X. Chen and D.–S. Xue, J. Magn. Magn. Mat. **512**, 167013 (2020).
 - [5] D. Wesenberg, A. Hojem, R. K. Bennet and B. L. Zink, J. Phys. D: Appl. Phys. **51** 244005 (2018)
 - [6] H. Yu, S. D. Brechet, J.-P. Ansermet, Phys. Lett. A **381**, 825-837 (2017)
 - [7] Fig. 8 and Tab. 2 in J. Hu, S. Granville, H. Yu, Ann. Phys., Lpz. **532**, 1900456 (2020)
 - [8] A. Sakai, Y. P. Mizuta, A. A. Nugroho, R. Sihombing, T. Koretsune, M.-T. Suzuki, N. Take-mori, R. Ishii, D. Nishio-Hamane, R. Arita, P. Goswami and S. Nakatsuji, Nat. Phys. **14**, 1119–1124 (2018)

- [9] H. Reichlova, R. Schlitz, S. Beckert, P. Sweekis, A. Markou, Y.-C. Chen, D. Kriegner, S. Fabretti, G. H. Park, A. Niemann, S. Sudheendra, A. Thomas, K. Nielsch, C. Felser, and S. T. B. Goennenwein, *Appl. Phys. Lett.* **113**, 212405 (2018)
- [10] I. Belopolski, K. Manna, D. S. Sanchez, G. Chang, B. Ernst, J. Yin, S. S. Zhang, T. Cochran, N. Shumiya, H. Zheng, B. Singh, G. Bian, D. Multer, M. Litskevich, X. Zhou, S.-M. Huang, B. Wang, T.-R. Chang, S.-Y. Xu, A. Bansil, C. Felser, H. Lin, and M. Z. Hasan, *Science* **365**, 1278 (2019).
- [11] G.-H. Park, H. Reichlova, R. Schlitz, M. Lammel, A. Markou, P. Sweekis, P. Ritzinger, D. Kriegner, J. Noky, J. Gayles, Y. Sun, C. Felser, K. Nielsch, S. T. B. Goennenwein, and A. Thomas, *Phys. Rev. B* **101** (2020)
- [12] T. Graf, C. Felser, S. S. P. Parkin, *Prog. Solid. State Ch.* **39**, 1-50 (2011)
- [13] N. H. Protik and D. A. Broido, *Phys. Rev. B* **101**, 075202 (2020)
- [14] Md. M. H. Polash, F. Mohaddes, M. Rasouljanboroujeni, D. Vashae, *J. Mater. Chem. C* **8**, 4049-4057 (2020)
- [15] A. W. Rushforth, K. Výborný, C. S. King, K. W. Edmonds, R. P. Champion, C. T. Foxon, J. Wunderlich, A. C. Irvine, P. Vašek, V. Novák, K. Olejník, Jairo Sinova, T. Jungwirth, and B. L. Gallagher, *Phys. Rev. Lett.* **99**, 147207 (2007)
- [16] W. Döring, *Ann. Phys., Lpz.* **424**, 259 (1938)
- [17] E. De Ranieri, A. W. Rushforth, K. Výborný, U. Rana, E. Ahmad, R. P. Champion, C. T. Foxon, B. L. Gallagher, A. C. Irvine, J. Wunderlich, *New J. Phys.* **10**, 065003 (2008)
- [18] V. D. Ky, *Phys. Status Solidi B* **17**, K207 (1966).
- [19] G. J. Snyder and E. S. Toberer, *Nat. Mater.* **7**, 105–114 (2008)
- [20] T. Janda, J. Godinho, T. Ostatnicky, E. Pfitzner, G. Ulrich, A. Hoehl, S. Reimers, Z. Šobáň, T. Metzger, H. Reichlová, V. Novák, R. P. Champion, J. Heberle, P. Wadley, K. W. Edmonds, O. J. Amin, J. S. Chauhan, S. S. Dhesi, F. Maccherozzi, R. M. Otxoa, P. E. Roy, K. Olejník, P. Nemeč, T. Jungwirth, B. Kaestner, and J. Wunderlich, *Phys. Rev. Materials* **4**, 094413 (2020)
- [21] O.M.Løvvik, Espen Flage-Larsen, and Gunstein Skomedal, *J. Appl. Phys.* **128**, 125105 (2020)
- [22] Electronic bands in the bulk can be characterised by topological invariants which indicate whether or not there will be surface states. These are related to Berry curvature, a quantity related to ANE [8], through Eq. 2 of J. Kübler and C. Felser, *Europhys. Lett.* **114**, 47005

- (2016).
- [23] A. Sakai, S. Minami, T. Koretsune, T. Chen, T. Higo, Y. Wang, T. Nomoto, M. Hirayama, S. Miwa, D. Nishio-Hamane, F. Ishii, R. Arita and S. Nakatsuji, *Nature* **581**, 53 (2020)
 - [24] W. Limmer, J. Daeubler, L. Dreher, M. Glunk, W. Schoch, S. Schwaiger, and R. Sauer, *Phys. Rev. B* **77**, 205210 (2008).
 - [25] M. Althammer, doctoral thesis, Technische Universität München, 2012
 - [26] O. Reimer, D. Meier, M. Bovender, L. Helmich, J.-O. Dreessen, J. Kriefft, A. S. Shestakov, C. H. Back, J.-M. Schmalhorst, A. Hütten, G. Reiss and T. Kuschel, *Sci. Rep.* **7**, 40586 (2017)
 - [27] P.B.Jayathilaka, D.D.Belyea, T.J.Fawcett, and Casey W.Miller, *J. Magn. Magn. Mat.* **382**, 376 (2015).
 - [28] T. Janda, J. Godinho, T. Ostatnicky, E. Pfitzner, G. Ulrich, A. Hoehl, S. Reimers, Z. Šobán, T. Metzger, H. Reichlová, V. Novák, R. P. Champion, J. Heberle, P. Wadley, K. W. Edmonds, O. J. Amin, J. S. Chauhan, S. S. Dhese, F. Maccherozzi, R. M. Otxoa, P. E. Roy, K. Olejník, P. Nemeč, T. Jungwirth, B. Kaestner, and J. Wunderlich, *Phys. Rev. Materials* **4**, 094413 (2020)
 - [29] A. D. Avery, M. R. Pufall, and B. L. Zink, *Phys. Rev. Lett.* **109**, 196602 (2012)
 - [30] A. Markou, D. Kriegner, J. Gayles, L. Zhang, Y.-C. Chen, B. Ernst, Y.-H. Lai, W. Schnelle, Y.-H. Chu, Y. Sun, and C. Felser, *Phys. Rev. B* **100**, 054422 (2019)
 - [31] U. Pietsch, V. Holý, and T. Baumbach, *High-resolution X-ray Scattering: From Thin Films to Lateral Nanostructures* (Springer, New York, 2004).
 - [32] W. Limmer, M. Glunk, J. Daeubler, T. Hummel, W. Schoch, R. Sauer, C. Bihler, H. Huebl, M. S. Brandt, and S. T. B. Goennenwein, *Phys. Rev. B* **74**, 205205 (2006)
 - [33] E. C. Stoner and E. P. Wohlfarth, *Phil. Trans. Roy. Soc. A* **240**, 599 (1948).
 - [34] P. Swekis, A. S. Sukhanov, Y.-C. Chen, A. Gloskovskii, G. H. Fecher, I. Panagiotopoulos, V. Ukleev, A. Devishvili, A. Vorobiev, D. S. Inosov, S. T. B. Goennenwein, C. Felser and A. Markou (unpublished)
 - [35] A tensor representing a macroscopic physical property of a crystal must be invariant under all symmetry operations of the corresponding point-group.
 - [36] C. Zener, *Phys. Rev.* **96**, 1335 (1954).
 - [37] M. Tsunoda, H. Takahashi, S. Kokado, Y. Komasaki, A. Sakuma and M. Takahashi, *Appl. Phys. Express* **3**, 113003 (2010)

- [38] I. Turek, J. Kudrnovský, and V. Drchal, *Phys. Rev. B* **86**, 014405 (2012).
- [39] T. Sato, S. Kokado, M. Tsujikawa, T. Ogawa, S. Kosaka, M. Shirai and M. Tsunoda, *Appl. Phys. Express* **12**, 103005 (2019)
- [40] P. Ritzinger, master thesis, Technische Universität Dresden, 2020
- [41] S. Kokado and M. Tsunoda, *J. Phys. Soc. Jpn.* **84**, 094710 (2015).
- [42] S. N. Guin, K. Manna, J. Noky, S. J. Watzman, C. Fu, N. Kumar, W. Schnelle, C. Shekhar, Y. Sun, J. Gooth, and C. Felser, *NPG Asia Mater.* **11**:16 (2019)
- [43] B. Balke, S. Ouardia, T. Graf, J. Barth, C. G. F. Blum, G. H. Fecher, A. Shkabko, A. Weidenkaff, C. Felser, *Sol. St. Comm.* **150**, 529 (2010).
- [44] C. S. Lue and Y.-K. Kuo, *Phys. Rev. B* **66**, 085121 (2002).
- [45] L. Smrčka and P. Vašek, *Czech. J. Phys. B* **26**, 1137–1147 (1976)
- [46] T. Miyasato, N. Abe, T. Fujii, A. Asamitsu, S. Onoda, Y. Onose, N. Nagaosa, and Y. Tokura, *Phys. Rev. Lett.* **99**, 086602 (2007)
- [47] S. J. Watzman, R. A. Duine, Y. Tserkovnyak, S. R. Boona, H. Jin, A. Prakash, Y. Zheng, and J. P. Heremans, *Phys. Rev. B* **94**, 144407 (2016)

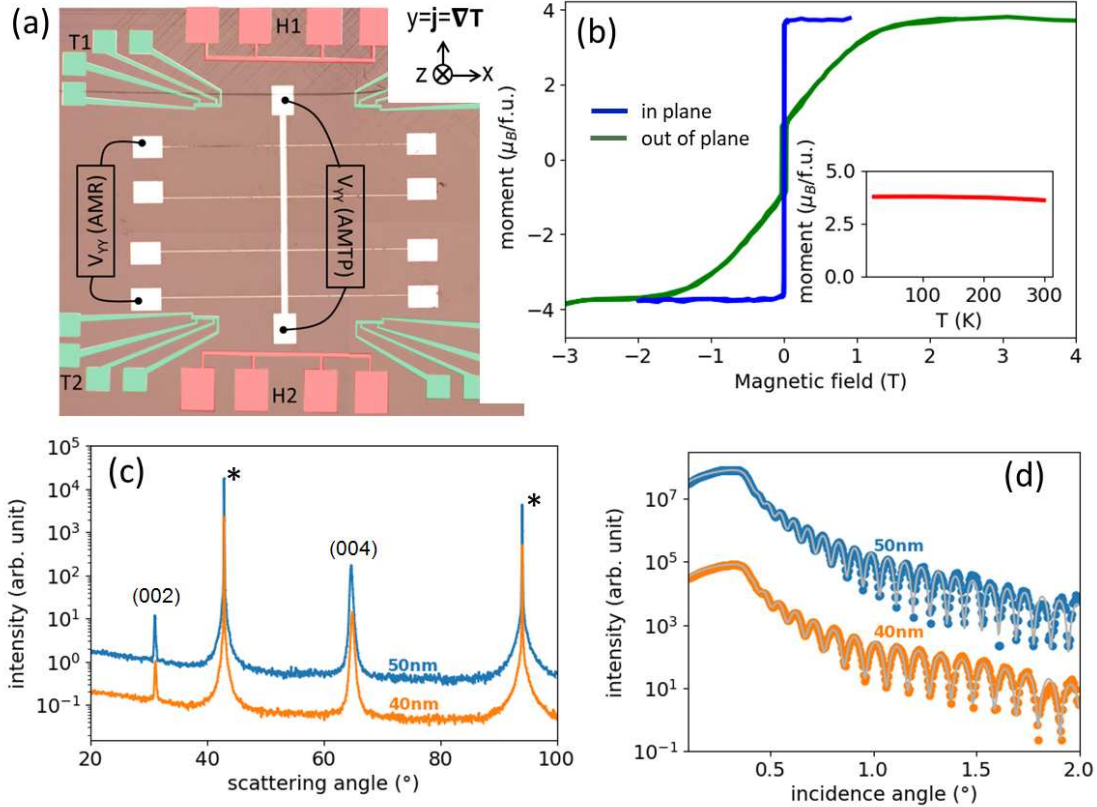


FIG. 1. Sample characterization. a) Schematic image of the sample. The white areas are Co_2MnGa . V_{xx} (AMR) are the contacts used for measuring voltage in the AMR experiment, while the current I was applied between V_{xx} (AMTP). In the AMTP experiment, the voltage was measured at V_{xx} (AMTP). The red colored areas are Pt wires which are used in the AMTP experiments as on-chip heater and thermometer (green). b) in-plane and out-of-plane measurement of the magnetization vs. applied magnetic field. The inset shows the magnetization vs. temperature. The saturated magnetic moment is approx. $4\mu_B$ per formula unit. c) X-ray diffraction radial scans of Co_2MnGa films with 40 and 50nm thickness. Bragg peaks labeled by an asterisk (*) originate from the (00L) series of the MgO substrate, while Bragg peaks of Co_2MnGa are labeled by their Miller indices. d) X-ray reflectivity pattern of the 40 nm and 50 nm thick Co_2MnGa films. Experimental data are shown as data points, while the solid line represents a model fit based on the extended Parratt formalism.

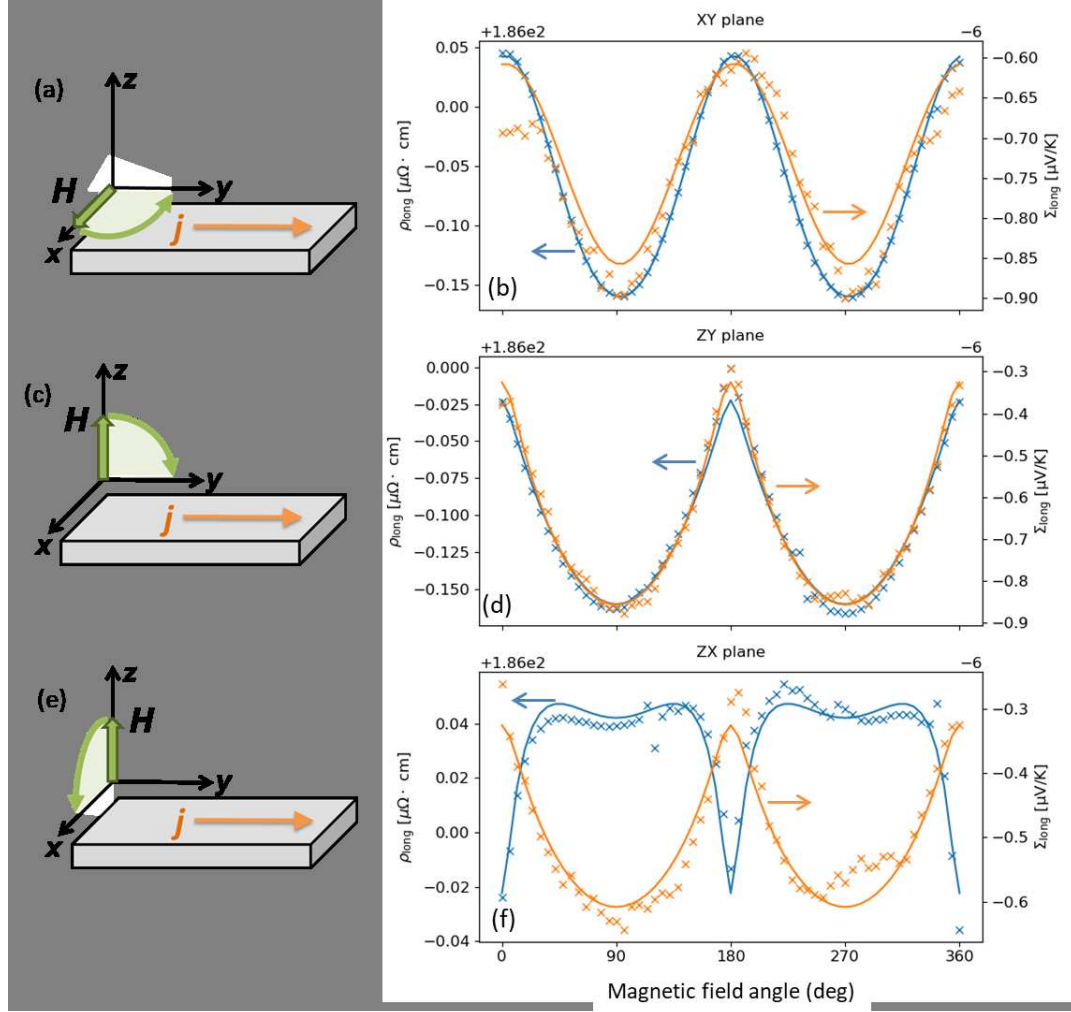


FIG. 2. Results of the AMR and AMTP measurement (crosses) and fitting (continuous lines) in the 50 nm sample at 300 K (AMR) and 250 K (AMTP). a) b), c) Schematic sketch of the magnetic field rotation in the XY, ZY, ZX plane with respect to the coordinate system and the sample. d), e), f) AMR (blue, left y-axes) and AMTP (orange, right y-axes) results; note the shifts of vertical axes indicated at the top of each panel: minimum resistivity, which occurs for $\mathbf{m} \parallel \mathbf{j}$, is $171 \mu\Omega \cdot \text{cm}$.

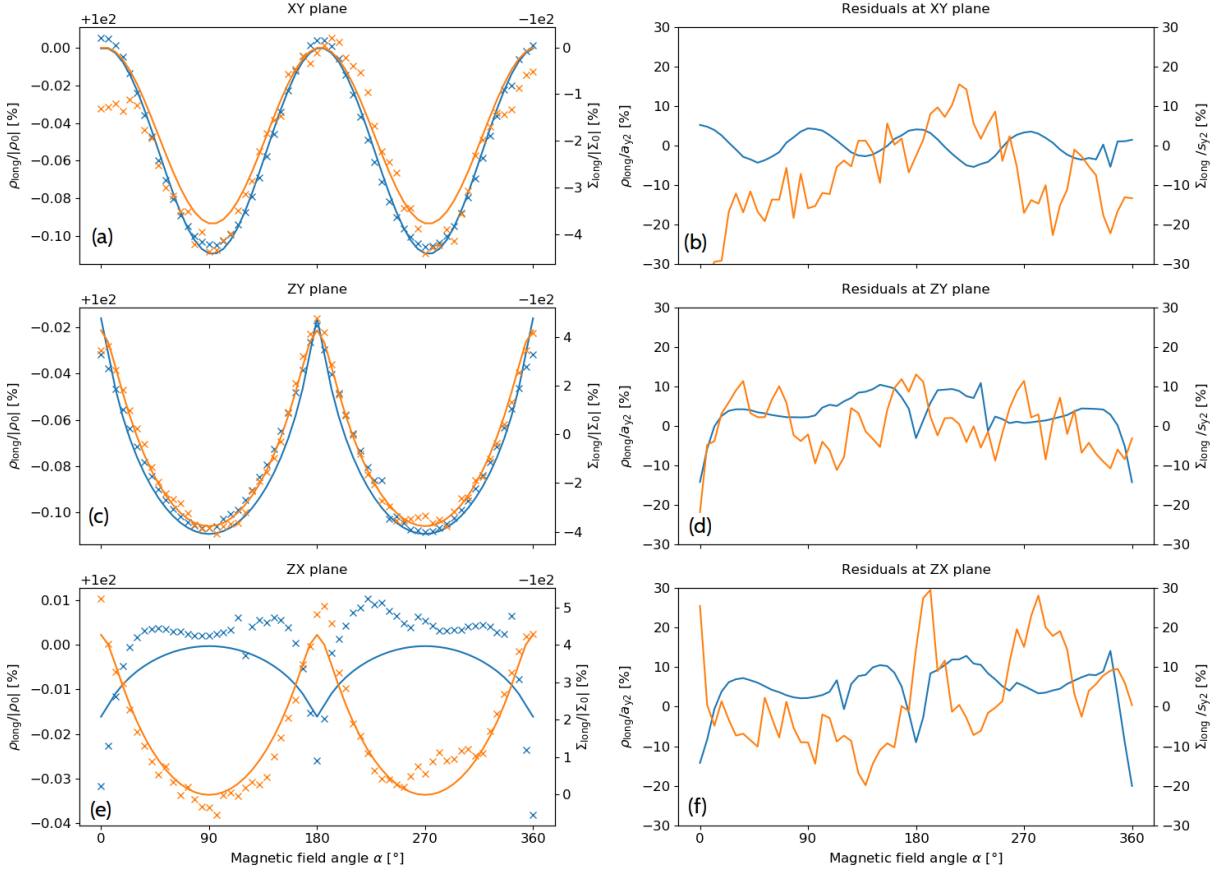


FIG. 3. (a,c,e) Data from Fig. 2 where AMR (AMTP) is fitted by Eq. 4 (Eq. 5, respectively) with second-order terms only; a lower quality, compared to Fig. 2(f), of the AMR fit in the bottom panel is clearly apparent but systematic deviations can also be observed for the XY and ZY rotations. (b,d,f) The difference of the experimental data and fits on the left (fit residuals), see text for a detailed discussion.

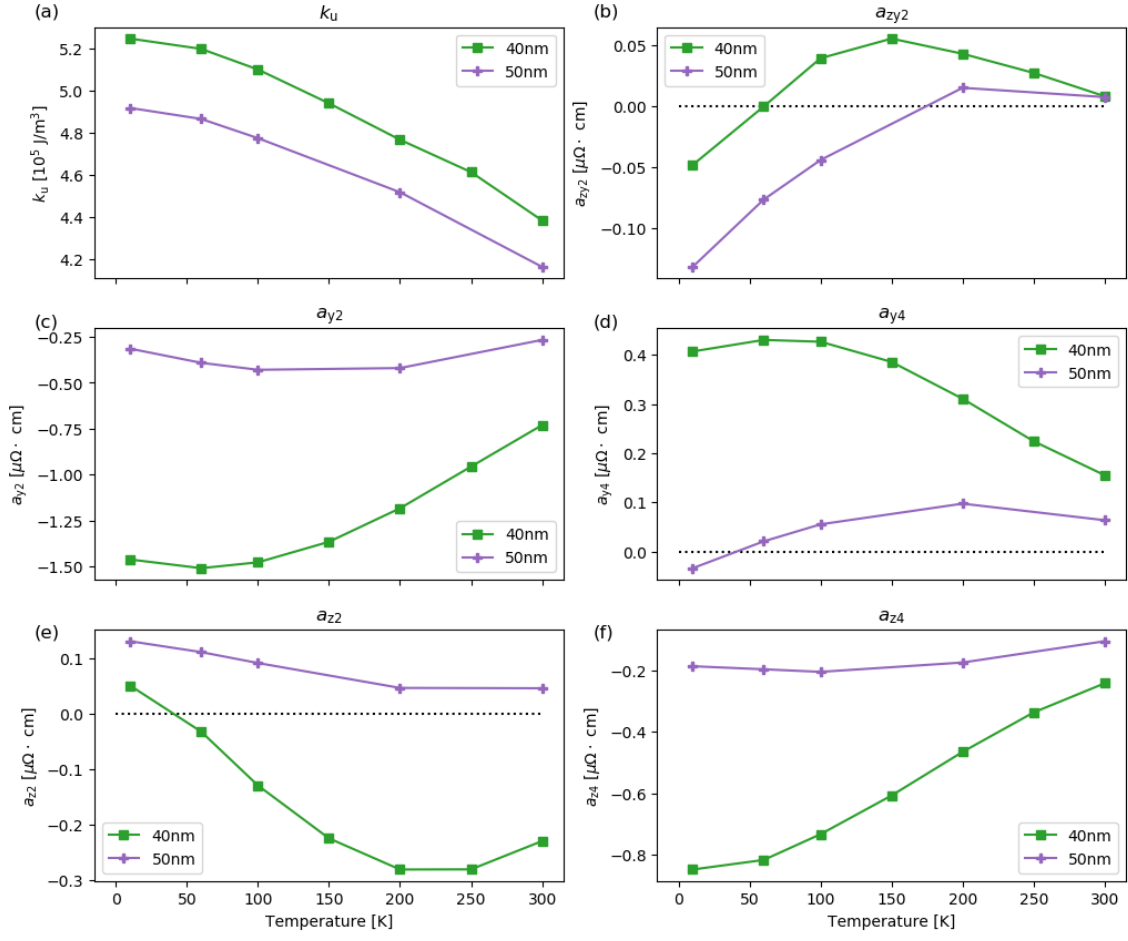


FIG. 4. Temperature evolution of the parameters obtained by the phenomenological fit to AMR data. (A) Uniaxial magnetic anisotropy, (B-F) parameters for AMR defined in Eq. 4.

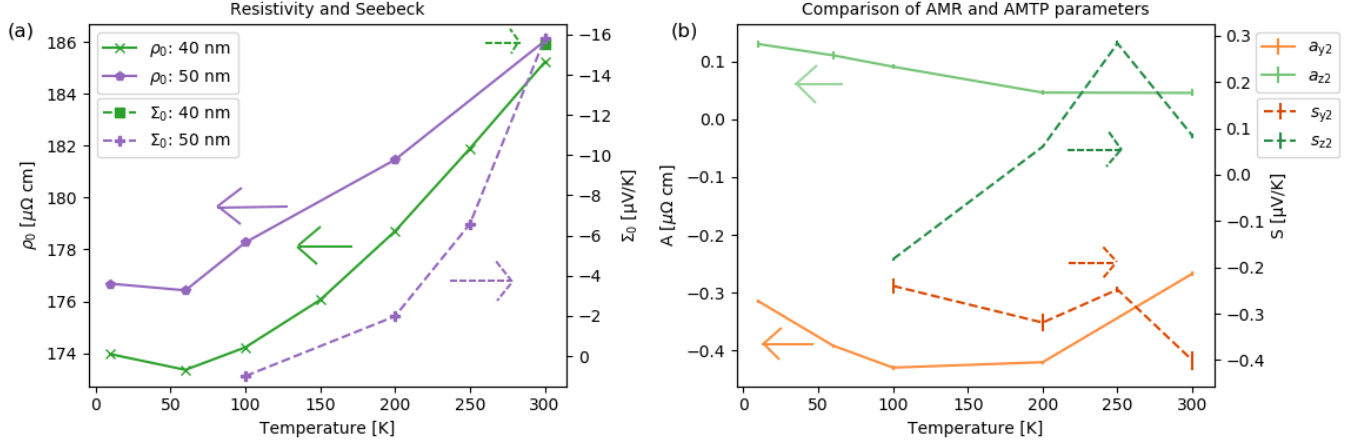


FIG. 5. a) Longitudinal Seebeck coefficient Σ_0 as a function of the temperature. The different samples are distinguished by the shape of symbols. The absolute value of the Seebeck coefficient of the 50 nm sample is monotonously increasing with temperature. There is a sign change at low temperatures. The Seebeck coefficients at $T = 300$ K for the 40 and 50 nm sample are of comparable magnitude. b) Comparison of the AMTP and the corresponding AMR parameters in the 50 nm sample as a function of temperature. AMR and AMTP are distinguished by linestyle. The m_y^2 contributions are in shades of orange, the m_z^2 contributions in shades of green. They do not seem to follow any common trend. Error bars of AMTP and AMR parameters in b) (implied by the fitting procedure) are too small to be visually resolved.